^{129}Xe-Cs (D_1, D_2) versus ^{129}Xe-Rb (D_1) spin-exchange optical pumping at high xenon densities using high-power laser diode arrays

Nicholas Whiting,[*] Neil A. Eschmann,[†] and Boyd M. Goodson[‡]
Department of Chemistry and Biochemistry, Southern Illinois University, Carbondale, Illinois 62901, USA

Michael J. Barlow
Sir Peter Mansfield Magnetic Resonance Centre, University of Nottingham, Nottingham, NG7 2RD, UK
(Received 20 November 2010; revised manuscript received 31 March 2011; published 26 May 2011)

We investigate ^{129}Xe-Cs (D_1, D_2) spin exchange optical pumping (SEOP) at high Xe densities (∼0.12–2.44 amagat) using newly available high-power (>40 W) laser diode arrays and compare with ^{129}Xe-Rb D_1 SEOP under similar conditions. At elevated Xe densities, the spin-exchange rate (per alkali-metal atom, γ') for Cs-^{129}Xe is ∼1.5-fold greater than that for Rb-^{129}Xe. Higher spin-exchange rates and lower ^{129}Xe spin-destruction rates for Cs-^{129}Xe versus Rb-^{129}Xe contribute to ∼twofold improvement in ^{129}Xe nuclear spin polarization measured at 9.4 T—with the largest gains observed at the highest Xe densities.

DOI: 10.1103/PhysRevA.83.053428 PACS number(s): 32.80.Xx, 42.55.Px, 82.56.−b, 87.61.−c

I. INTRODUCTION

The high nuclear spin polarization of hyperpolarized (HP) noble gases (e.g., ^{3}He and ^{129}Xe) has been exploited for a wide range of applications, from magnetic resonance spectroscopy and imaging [1] to fundamental physics experiments [2]. While ^{3}He has a larger magnetic moment and a higher diffusivity (useful for probing lung pathologies [3]), ^{129}Xe offers greater chemical shift sensitivity and proclivity for interacting with molecular and materials surfaces. Moreover, ^{129}Xe is relatively abundant; thus, the world-wide ^{3}He shortage [4] provides further urgency for the development of improved HP ^{129}Xe approaches.

HP ^{129}Xe is typically produced via spin-exchange optical pumping (SEOP) with an alkali-metal vapor [5,6]. Rubidium has been the alkali metal of choice for HP gas preparation because of its large spin-exchange cross sections [5], relatively high vapor pressures, and the abundance of inexpensive, high-power light sources (i.e., laser diode arrays, LDAs) that emit at its *D*-line absorption wavelengths [7]. Nevertheless, there may be advantages to using *cesium* for SEOP: for example, the Cs-^{129}Xe binary spin-exchange cross section has been measured to be ∼1.9 times greater than that of Rb-^{129}Xe [8], while the Cs-^{129}Xe collisional spin-destruction cross section (which quantifies the loss of electron spin polarization with increasing Xe density) may be only half that of Rb-^{129}Xe [9,10]. Additionally, Cs has even higher vapor pressures [11], lower-energy *D* lines (giving more photons per watt of light) [12], and greater *D*-line spacing [13]. Yet despite these anticipated advantages and considerable effort (e.g., Refs. [12,14,15]), improved results with Cs have yet to be realized and Cs-^{129}Xe SEOP is still not widely practiced. Indeed, the development of Cs-^{129}Xe SEOP has been hindered by the lack of available high-power light sources that emit at the Cs *D* lines (equivalent to those available for Rb [8]), preventing the proper exploration of the SEOP parameter space [16]—and hence, limiting the xenon polarization that can be achieved.

In this work, we investigate ^{129}Xe-Cs SEOP using newly available high-power LDAs that emit at the Cs D_1 or D_2 lines, and compare with ^{129}Xe-Rb D_1 SEOP performed under similar conditions. At elevated Xe densities (∼0.61–2.44 amagat [17], or 100–2000 Torr), the per-atom spin-exchange rate for Cs-^{129}Xe is ∼1.5-fold greater than that for Rb-^{129}Xe—in good agreement with previous measurements [8,18]. Higher spin-exchange rates and lower ^{129}Xe spin-destruction rates for Cs-^{129}Xe versus Rb-^{129}Xe contribute to a twofold average improvement in ^{129}Xe spin polarization (P_{Xe}) measured at 9.4 T—with the largest gains observed at the highest Xe densities.

II. METHODS

Aspects of our SEOP apparatus have been described previously [16,19]. Briefly, "batch-mode" SEOP was performed using Surfasil-coated Rosen [20] cells [Pyrex, 75 cm^3, 1-in. outer diameter (o.d.) inner cell per cylinder, 2-in. o.d. outer cylinder]; in the Rosen cell design, the inner cell volume contains the alkali metal and the gases under study, whereas the outer volume is used as a forced-air oven to heat the contents of the inner cell. Each Rosen cell was loaded with either Rb or Cs and variable Xe-N_2 mixtures [21] and illuminated with broadband $Al_xGa_{1-x}As$ LDAs (QPC, Sylmar, CA) tuned to the Cs ($D_1 = 894.3$ nm or $D_2 = 852.1$ nm) or Rb ($D_1 = 794.8$ nm) lines. Nominal laser conditions (Fig. 1) for Cs D_1 were ∼46 W, $\Delta\lambda_{fwhm} = 2.9$ nm; for Cs D_2 they were ∼40 W, $\Delta\lambda_{fwhm} = 1.9$ nm; and for Rb D_1 they were ∼53 W, $\Delta\lambda_{fwhm} = 2.1$ nm. The LDAs were mounted to water-cooled plates and driven with Xantrex power supplies (6 V, 110 A for the Cs lasers, 12 V, 70 A for the Rb laser). The laser output is fiber-coupled into a home-built monocular circular polarizer box (with broadband near-IR optics comprising a collimating lens, a corner-cube, a rotatable quarter-wave plate,

[*]Current address: SPMMRC, University of Nottingham, Nottingham, NG7 2RD, UK.
[†]Current address: Chemistry Department, University of California, Santa Barbara, CA.
[‡]bgoodson@chem.siu.edu

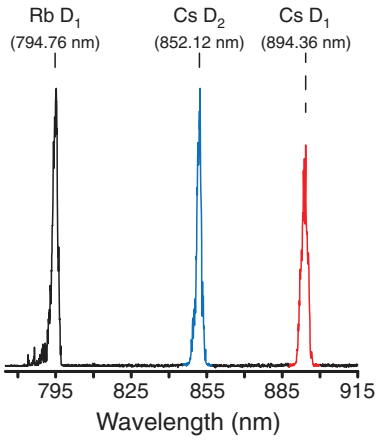

FIG. 1. (Color online) Composite figure comprising separate spectra of three high-power broadband LDAs emitting at the Rb D_1, Cs D_2, and Cs D_1 absorption lines, respectively. Laser characteristics (left to right) are ~795 nm, ~100 W, $\Delta\lambda_{\mathrm{fwhm}} = 2.3$ nm; ~852 nm, ~48 W, $\Delta\lambda_{\mathrm{fwhm}} = 1.9$ nm; ~894 nm, ~46 W, $\Delta\lambda_{\mathrm{fwhm}} = 2.9$ nm. (Due to its higher power, the Rb laser's spectrum is normalized to that of the Cs D_2 laser; however, laser powers around ~50 W were used for the experiments reported here.)

and a beam dump). The short (30 cm) polarization-preserving fiber retains most of the linear polarization of the emitted laser light, resulting in an efficient (~90/10) straight or angled beam ratio (the "angled" beam is directed into the beam dump, whereas the "straight" beam is delivered to the cell; this design mitigates the issue of off-axis pumping [22], which may confound studies utilizing binocular optics for circularly polarizing the LDA output). A 2-in. mirror mounted behind the cell retroreflects transmitted laser light back into the cell; each laser's transmitted spectral profile is monitored by a high-resolution near-IR spectrometer (Ocean Optics) via an optical fiber probe mounted just behind the mirror. The cell resides in a Helmholtz coil (HC) pair [22-in. inner diameter (i.d.), ~32 G] and is supported and positioned with custom (nonmagnetic) polytetrafluoroethylene (PTFE) mounts and Garolite posts on translation stages.

^{129}Xe polarization dynamics were monitored *in situ* using a low-field NMR spectrometer (Magritek Aurora; nominal ^{129}Xe NMR frequency of 37.5 kHz) and a home-built detection coil (with a noise-suppressing counter-wound bucking coil [23]). Low-field NMR signals were acquired with a single rf pulse following rezeroing P_{Xe} (via the application of ~300–500 "crusher" pulses) and subsequent laser illumination of the cell for a variable time. For high-field NMR measurements, hyperpolarized xenon was collected following SEOP at optimal temperatures (T_{OPT} [24]) by expanding the contents of the cell into a pre-evacuated volume that includes a stopcock-sealed NMR tube. ^{129}Xe NMR spectra were recorded via the application of a single (1 μs, 6.7° tipping angle) rf pulse following transfer to 9.4 T using a Varian Inova spectrometer. The absolute P_{Xe} value was determined via comparison with a thermally polarized ^{129}Xe NMR signal from the same sample [obtained following careful addition of sufficient O_2 gas to reduce the ^{129}Xe T_1 (to a few seconds) to permit signal averaging].

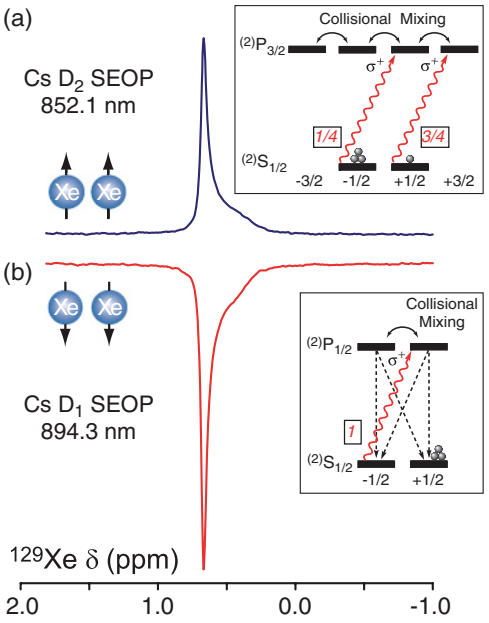

FIG. 2. (Color online) Examples of HP ^{129}Xe NMR spectra (at 9.4 T, phase-referenced to an absorptive thermally-polarized ^{129}Xe NMR signal) obtained following ^{129}Xe-Cs D_2 (a) or D_1 (b) SEOP using the same light helicity. Both spectra are frequency-referenced to the chemical shift (δ) of ^{129}Xe gas extrapolated to zero pressure (with the asymmetry of the line shapes resulting simply from magnetic field inhomogeneities, which is not relevant to the present study). Insets: Corresponding transitions for D_2 and D_1 OP assuming σ^+ CP light (neglecting nuclear contributions, with excited-state relaxation shown as dashed lines—omitted in the D_2 diagram for simplicity).

III. RESULTS AND DISCUSSION

A. ^{129}Xe-Cs SEOP: D_1 versus D_2 excitation

Examples of high-field HP ^{129}Xe NMR spectra obtained following ^{129}Xe-Cs D_2 or D_1 SEOP are shown in Fig. 2. Unlike with D_1 excitation, D_2 pumping drives population from both ground-state sublevels (with repopulation via relaxation at effectively equal rates because of collisional mixing of the excited states [25]). However, the ground-state sublevels are depopulated at a 1:3 ratio [25,26]; thus, the alkali-metal electron spin polarization ($|P_{\mathrm{AM}}|$) can theoretically approach 0.5 for D_2 optical pumping (OP) (cf. a limit of $|P_{\mathrm{AM}}| = 1$ for D_1 OP). Thus, significant ^{129}Xe polarization can still be achieved using Cs SEOP at the D_2 line [14]. Greater light absorption at the D_2 line caused by the twofold higher oscillator strength [27] gives rise to lower optimal cell temperature (T_{OPT}) values [24] when switching from D_1 to D_2 SEOP. Because of the 1:3 depopulation ratio, performing SEOP at the D_2 versus the D_1 Cs line—but with the same light helicity—polarizes the ^{129}Xe in the opposite direction (Fig. 2). This effect also illustrates the source of concern regarding inadvertent D_2 pumping when performing rubidium D_1 SEOP with broadband sources [10,13,28], as any light absorbed at the wing of the D_2 line would tend to depolarize the noble gas.

B. Low-field measurements of ^{129}Xe-Cs and ^{129}Xe-Rb spin exchange and ^{129}Xe spin destruction

The availability of LDAs with emission at the Cs (D_1 and D_2) and Rb (D_1) lines allows direct comparison of SEOP phenomena under otherwise similar conditions. Low-field *in situ* ^{129}Xe NMR buildup curves were obtained for various cell temperatures ($T_{\rm cell}$) and Xe densities [e.g., Fig. 3(a)] and were fit to an exponential [29]:

$$S(t) = S_\infty[1 - \exp(-\Gamma t)], \tag{1}$$

where the time constant is given by $\Gamma = \gamma_{\rm SE} + \Gamma_{\rm Xe}$, $\gamma_{\rm SE}$ is the spin-exchange rate, $\Gamma_{\rm Xe}$ is the ^{129}Xe nuclear spin-destruction rate ($=1/T_1^{\rm Xe}$), and S_∞ is the steady-state low-field ^{129}Xe NMR signal, given by

$$S_\infty \propto P_{\rm Xe} = \langle P_{\rm AM}\rangle \frac{\gamma_{\rm SE}}{\Gamma}. \tag{2}$$

A linear fit of Γ values plotted versus the alkali-metal density ([AM]) should provide measures of the per-atom spin-exchange rate ($\gamma' = \gamma_{\rm SE}/[{\rm AM}]$) and the ^{129}Xe spin-destruction rate ($\Gamma_{\rm Xe}$) from the slope and y intercept, respectively [29] [Figs. 3(b) and 3(c)]. Here, alkali-metal densities are estimated from vapor-pressure curves [27,30].

As discussed below, a significant dependence upon the Xe density ([Xe]) was not expected under our conditions—as confirmed for Rb [Fig. 3(b); see also Fig. 4]. Indeed, the Rb data can be fit in aggregate to obtain overall "average" values of $\gamma' = 1.67 \pm 0.06 \times 10^{-15}$ cm^3/s and $\Gamma_{\rm Xe} = 3.4 \pm 0.2 \times 10^{-3}$ s^{-1}. The Cs data exhibit not only a steeper dependence upon the alkali-metal density but also a larger spread resulting from an apparent dependence of spin-exchange rate upon the Xe density. (^{129}Xe spin destruction does not show a clear [Xe] dependence.) In part because ^{129}Xe spin destruction is much slower for Cs than Rb, fitting the Cs data in aggregate requires fixing $\Gamma_{\rm Xe}$ (here set to $4 \pm 3 \times 10^{-4}$ s^{-1}, the average obtained from separate fits for each Xe density)—yielding $\gamma' = 2.6 \pm 0.1 \times 10^{-15}$ cm^3/s (~1.5-fold greater than for Rb). Plots of the per-atom spin-exchange rate versus Xe partial pressure for Cs D_1, Cs D_2, and Rb D_1 SEOP are shown in Fig. 4. The dependence for the Rb data is relatively flat; however, both sets of Cs data exhibit per-atom spin-exchange rates similar to those of Rb at low Xe partial pressures, but significantly greater values at higher Xe pressures ($\gtrsim$500 Torr)—again, giving an average ratio of $\gamma'_{\rm CsXe}/\gamma'_{\rm RbXe} \sim 1.5$ over this range [31].

This ratio is in good agreement with recent measurements of Cs-^{129}Xe and Rb-^{129}Xe spin exchange performed under internally comparable conditions [8,18], but a more detailed interpretation is complicated by several factors. For example, the per-atom spin-exchange rates (γ') in Fig. 4, while in the range of previous measurements [5,8,18,29,32,33], are higher than recently reported values. The alkali-metal densities in Fig. 4 were calculated from oven air temperatures [27,29,30]; however, values predicted from empirical curves can deviate systematically from direct measurements [8,18,22]. In previous studies using Rosen cells [16], we found a 13°C–15°C difference between the temperatures of the oven air exhaust and the (hotter) outer wall of the cell during SEOP. Accounting for this difference reduces the per-atom spin-exchange rates by ~2.3-fold (more in line with expectations)—but importantly has little effect on the $\gamma'_{\rm CsXe}/\gamma'_{\rm RbXe}$ ratio.

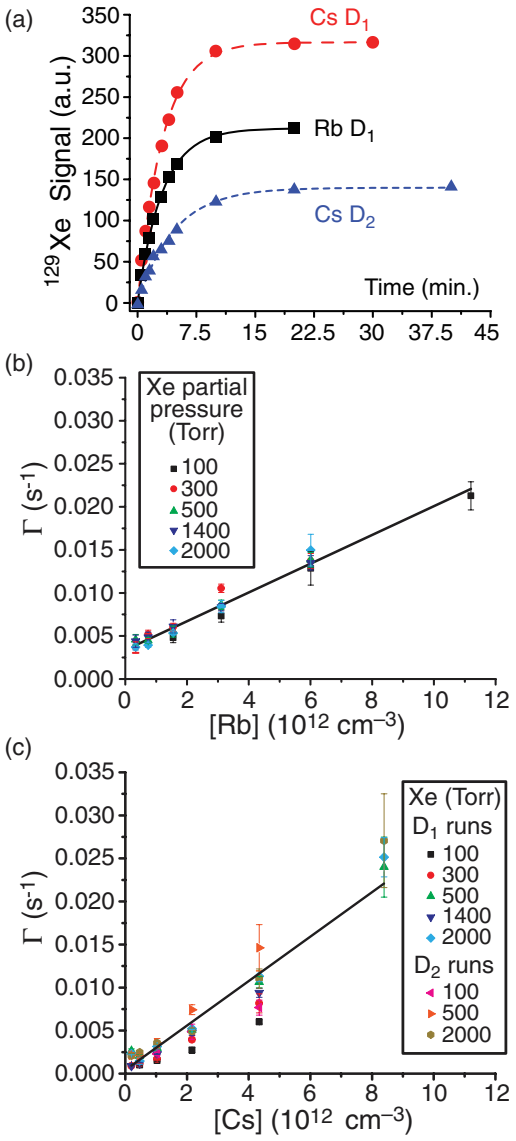

FIG. 3. (Color online) (a) Selected $P_{\rm Xe}$ buildup curves obtained during ^{129}Xe-Cs or ^{129}Xe-Rb SEOP (2000 Torr Xe, 600 Torr N_2). Cell temperatures (measured from oven air exhaust) and nominal laser conditions: 70°C and 46 W ($\Delta\lambda_{\rm fwhm} = 2.9$ nm) for Cs D_1; 60°C and 40 W ($\Delta\lambda_{\rm fwhm} = 1.9$ nm) for Cs D_2; and 80°C and 53 W ($\Delta\lambda_{\rm fwhm} = 2.1$ nm) for Rb D_1. Plots of Γ vs [Rb] (b) or [Cs] (c) (estimated from vapor-pressure curves [27]) for SEOP with various Xe densities; (c) contains Cs D_1 and D_2 SEOP results. Lines are fits to the aggregate data (see text).

Next, the per-atom spin-exchange rate is often partitioned as a sum of the binary spin-exchange cross section ($\langle\sigma v\rangle$, from two-body alkali-^{129}Xe collisions) and a three-body term given by $\gamma_M \zeta([{\rm Xe}] + b[{\rm N_2}])^{-1}$, where γ_M is the molecular spin-exchange rate, b is a factor that accounts for the presence of both Xe and N_2 in the cell (and their capacities to modulate the formation and breakup of transient alkali-^{129}Xe van der Waals complexes), and ζ is a parameter determined by the

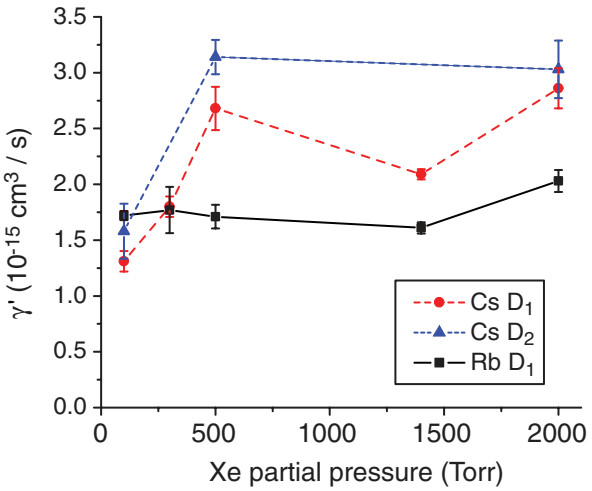

FIG. 4. (Color online) Plots of γ' vs Xe partial pressure for ^{129}Xe-Cs D_1 (red circles), ^{129}Xe-Cs D_2 (blue triangles), and ^{129}Xe-Rb D_1 SEOP (black squares). $[Xe] = 0.12$–2.44 amagat. The lines are to guide the eye.

relative abundances and nuclear spins of the involved alkali-metal isotopes (as well as by P_{AM} and the molecular lifetime) [5,18,29,34,35]. While the three-body term is expected to dominate at low total pressures (<hundreds of Torr), at sufficiently high pressures the molecular lifetimes should ultimately become short enough to reduce the spin-exchange rate to the ([Xe]-independent) two-body limit [8]. Happer and co-workers used high pressures (and high magnetic fields) to suppress the three-body contribution and obtain measurements of $\langle\sigma v\rangle_{CsXe} = 2.81 \times 10^{-16}$ cm^3/s and $\langle\sigma v\rangle_{RbXe} = 1.75 \times 10^{-16}$ cm^3/s at 9.4 T (giving $\gamma'_{CsXe}/\gamma'_{RbXe} \sim 1.6$) [8]. When extrapolated to low field, these values translate to 4.1×10^{-16} and 2.2×10^{-16} cm^3/s, respectively (giving a ratio of ~1.9). Hughes and co-workers performed experiments at low field and lower gas densities (~0.2–0.7 amagat) to measure both two-body and three-body spin-exchange contributions [18]; they reported per-atom spin-exchange rates of $\sim(1.9$–$5.4) \times 10^{-15}$ and $\sim(1.5$–$3.2) \times 10^{-15}$cm^3/s for Cs-^{129}Xe and Rb-^{129}Xe, respectively, corresponding to a range of $\gamma'_{CsXe}/\gamma'_{RbXe}$ ratios of ~1.2–1.7—again in good agreement with our results. However, the partitioning of their spin-exchange rates is surprising, with a large $\langle\sigma v\rangle_{RbXe}$ value ($\sim 1.0 \times 10^{-15}$ cm^3/s) and a >10-fold *smaller* $\langle\sigma v\rangle_{CsXe}$ value ($\sim 9.4 \times 10^{-17}$cm^3/s), that—when combined with relatively large values for b_{CsXe} and γ_M^{CsXe} of 0.97 and 4.92×10^5 s^{-1} (cf. 0.275 [29] and 1.02×10^5 s^{-1} for Rb-^{129}Xe)—translates to a disproportionately large contribution from the three-body term [18]. Thus, extrapolation to our (higher-pressure) conditions would predict the Cs-^{129}Xe spin-exchange rate to be >twofold *smaller* than that of Rb-^{129}Xe. Our γ'_{CsXe} values are sensitive to Xe density, but with the opposite trend. Given potential flaws in relaxation models involving transient van der Waals complexes [18,36], extrapolation of their results to our regime may be problematic. Measurements of higher per-atom spin-exchange rates with increasing Xe density have been reported previously [16,32], but they cannot be readily understood in terms of the current model [5,29]. In any case, for spin-exchange measurements obtained under comparable conditions, the $\gamma'_{CsXe}/\gamma'_{RbXe}$ ratio is arguably the most useful quantity for evaluating the utility of Cs-^{129}Xe SEOP because it avoids the above complications (as well as many systematic errors). While obtained in different regimes, the data from the present work and Refs. [8,18] indicate generally higher per-atom spin-exchange rates for Cs-^{129}Xe compared to Rb-^{129}Xe.

We also observed slower ^{129}Xe spin relaxation (Γ_{Xe}) in Cs- versus Rb-loaded cells. This effect is reminiscent of previous ^{3}He experiments [37] that found that Cs provided the longest ^{3}He T_1 values of all the coatings studied—several-fold longer than similar Rb-coated cells—and suggests that Cs coatings may be more effective at partitioning ^{129}Xe from paramagnetic centers near the cell's surfaces.

C. High-field measurements of P_{Xe}

Finally, the availability of LDAs that emit at the Cs and Rb D_1 lines—but with similar (high, ⩾40 W) output powers and linewidths—permits side-by-side comparison of Xe polarization under conditions relevant for enhanced NMR and MRI. A series of batch-mode SEOP runs were performed using Cs or Rb cells with variable Xe partial pressures; P_{Xe} values were measured via NMR following gas collection and transfer to high field (Fig. 5). ^{129}Xe polarization values achieved via Cs-^{129}Xe SEOP exceeded those obtained via Rb-^{129}Xe SEOP by an average of a factor of ~2—with the greatest improvements observed at the highest Xe densities (consistent with the $\gamma'_{CsXe}/\gamma'_{RbXe}$ trend in Fig. 4). The P_{Xe} values in Fig. 5 are plotted alongside estimates for the cell-averaged alkali-metal electron spin polarization ($\langle P_{AM}\rangle$). In addition to faster spin exchange, slower ^{129}Xe spin relaxation should cause P_{Xe} to track P_{AM} more closely for Cs (giving an edge over Rb even at the lowest Xe densities studied). The contributions from *alkali-metal* spin-destruction (Γ_{SD}) cannot be quantified without direct measurements of P_{AM}. However, given the similarities of the Cs-^{129}Xe and Rb-^{129}Xe OP conditions, the steeper fall-off in estimated $\langle P_{Rb}\rangle$ values with increasing Xe density would be consistent with predictions that $\Gamma_{SD}^{Rb} \gtrsim \Gamma_{SD}^{Cs}$ [9,10] (providing another potential advantage for using Cs for polarizing Xe—particularly at high Xe densities).

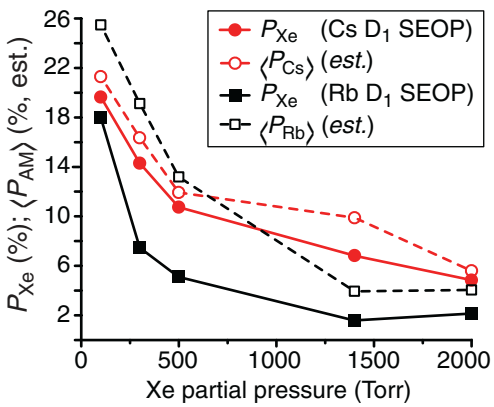

FIG. 5. (Color online) Plots of P_{Xe} vs Xe partial pressure following ^{129}Xe-Cs D_1 or ^{129}Xe-Rb D_1 SEOP and transfer to high field. LDA powers are 48 W (Cs) and 52 W (Rb). Estimates for $\langle P_{AM}\rangle$ are inferred from P_{Xe}, γ_{SE}, and Γ_{Xe} values and Eq. (2).

IV. SUMMARY

We have utilized newly available high-power broadband LDAs to investigate and compare ^{129}Xe-Cs and ^{129}Xe-Rb SEOP for HP ^{129}Xe generation. Higher spin-exchange rates and lower ^{129}Xe spin-destruction rates for Cs-^{129}Xe versus Rb-^{129}Xe contributed to a ∼twofold average improvement in P_{Xe}—with the largest gains observed at the highest Xe densities. We anticipate further gains with the advent of high-power *line-narrowed* LDAs [16,38] at Cs wavelengths. While the present results concern batch-mode ^{129}Xe SEOP, we expect they will also be relevant to other noble gas isotopes [39] and experimental configurations [6] and open a door to novel studies of alternate hybrid (e.g., Cs-Rb and Cs-K) cells. Thus, these results could have significant impact on a wide range of spectroscopic, biomedical imaging, and fundamental physics applications utilizing HP gases.

ACKNOWLEDGMENTS

We thank B. Driehuys for inspiration; X. Zhou and M. Rosen for helpful discussions; P. Nikolaou for assistance with OP cells; and G. Moroz for machining. This work was funded by NSF (CHE-03492550, DMR-0552800, and OISE-0966393), Research Corp., and SIU ORDA. M.J.B. is supported by the School of Medical & Surgical Sciences, University of Nottingham and GE Healthcare-Amersham.

[1] B. M. Goodson, J. Magn. Reson. **155**, 157 (2002); A. Bifone and A. Cherubini, Prog. Nucl. Magn. Reson. Spectrosc. **42**, 1 (2003).
[2] J. L. Friar, B. F. Gibson, G. L. Payne, A. M. Bernstein, and T. E. Chupp, Phys. Rev. C **42**, 2310 (1990); P. Anthony *et al.* (E124 Collaboration), Phys. Rev. Lett. **71**, 959 (1993); M. V. Romalis and M. P. Ledbetter, *ibid.* **87**, 067601 (2001).
[3] D. A. Yablonskiy *et al.*, J. Appl. Physiol. **107**, 8750 (2009).
[4] W. P. Halperin, Testimony to The House Committee on Science & Technology, Washington, DC (2010).
[5] W. Happer, E. Miron, S. Schaefer, D. Schreiber, W. A. vanWijngaarden, and X. Zeng, Phys. Rev. A **29**, 3092 (1984); X. Zeng, Z. Wu, T. Call, E. Miron, D. Schreiber, and W. Happer, *ibid.* **31**, 260 (1985); T. Walker and W. Happer, Rev. Mod. Phys. **69**, 629 (1997).
[6] B. Driehuys *et al.*, Appl. Phys. Lett. **69**, 1668 (1996); I. C. Ruset, S. Ketel, and F. W. Hersman, Phys. Rev. Lett. **96**, 053002 (2006).
[7] M. E. Wagshul and T. E. Chupp, Phys. Rev. A **40**, 4447 (1989).
[8] Y.-Y. Jau, N. N. Kuzma, and W. Happer, Phys. Rev. A **66**, 052710 (2002); **67**, 022720 (2003); **69**, 061401 (2004).
[9] T. G. Walker, Phys. Rev. A **40**, 4959 (1989); I. A. Nelson and T. G. Walker, *ibid.* **65**, 012712 (2001).
[10] A. H. Couture, T. B. Clegg, and B. Driehuys, J. Appl. Phys. **104**, 094912 (2008).
[11] The greater ease of vaporizing cesium at lower temperatures may be favorable for technical reasons [12]: For example, elevated cell temperatures can reduce the stability of organic coatings (often used on cell walls to decrease ^{129}Xe relaxation [41]) [42]; additionally, cell temperature stability and uniformity is often easier to maintain when operating closer to ambient conditions (and for stopped-flow SEOP [20], lower cell temperatures would generally enable faster apparatus cycling and hence greater production of HP Xe).
[12] D. Levron *et al.*, Appl. Phys. Lett. **73**, 2668 (1998).
[13] Rb-^{129}Xe SEOP may be impeded by inadvertent simultaneous pumping of the "red-side" wing of the D_2 line when using broadband sources tuned to the D_1 line [10,28] ($\Delta\lambda_{D1D2} \approx$ 15 nm; this effect could play a larger role at high xenon densities, as the D lines are shifted and asymmetrically broadened toward longer wavelengths [10,43]).
[14] J. Luo *et al.*, Appl. Magn. Reson. **17**, 587 (1999); X. Zhou *et al.*, Chin. Phys. Lett. **21**, 1501 (2004).
[15] B. Driehuys, in *American Physical Society Meeting: Division of Atomic, Molecular, and Optical Physics* (Charlottesville, VA, 2009).
[16] P. Nikolaou *et al.*, J. Magn. Reson. **197**, 249 (2009); N. Whiting *et al. ibid.* **208**, 298 (2011).
[17] 1 amagat = 2.6873×10^{19}cm^3, equal to the density of an ideal gas at 0°C and 760 Torr.
[18] W. Shao, G. Wang, and E. W. Hughes, Phys. Rev. A **72**, 022713 (2005).
[19] I. Saha *et al.*, Chem. Phys. Lett. **428**, 268 (2006).
[20] M. S. Rosen *et al.*, Rev. Sci. Instrum. **70**, 1546 (1999).
[21] For 100–1400 Torr Xe, N_2 was added to give 2000 Torr total pressure; for 2000 Torr Xe, 600 Torr N_2 was added.
[22] B. Chann, E. Babcock, L. W. Anderson, and T. G. Walker, Phys. Rev. A **66**, 033406 (2002).
[23] N. Whiting, P. Nikolaou, N. Eschmann, M. Barlow, and B. Goodson, in *50th Experimental Nuclear Magnetic Resonance Conference* (Pacific Grove, CA, 2009).
[24] T_{OPT} was determined for each Xe density (∼60°C–65°C, ∼70°C, and ∼85°C–90°C for Cs D_2, Cs D_1, and Rb D_1 SEOP, respectively). While we have found an interplay between T_{OPT} and [Xe] using *narrowed* high-power LDAs for Rb [16], here T_{OPT} varied $\lesssim$5°C using broadband LDAs.
[25] J. Fricke *et al.*, Phys. Rev. **163**, 45 (1967).
[26] G. D. Domenico and A. Weis, Wolfram Demonstrations Project [http://demonstrations.wolfram.com/TransitionStrengthsOfAlkaliMetalAtoms/].
[27] D. A. Steck [http://steck.us/alkalidata], rev. 2.1.2 (2009).
[28] E. Babcock, I. Nelson, S. Kadlecek, B. Driehuys, L. W. Anderson, F. W. Hersman, and T. G. Walker, Phys. Rev. Lett. **91**, 123003 (2003).
[29] G. D. Cates, R. J. Fitzgerald, A. S. Barton, P. Bogorad, M. Gatzke, N. R. Newbury, and B. Saam, Phys. Rev. A **45**, 4631 (1992).
[30] The relative values of [Cs] and [Rb] in Fig. 3 are qualitatively supported by laser-transmittance measurements.
[31] The spin-exchange rate should not depend upon the excitation pathway; thus small differences in γ' for Cs-^{129}Xe D_1 and D_2 SEOP are not considered significant.
[32] M. P. Augustine and K. W. Zilm, Mol. Phys. **89**, 737 (1996); Chem. Phys. Lett. **280**, 24 (1997).
[33] C. V. Rice and D. Raftery, J. Chem. Phys. **117**, 5632 (2002).

[34] In general, ζ has a complex analytical form; In the "short" molecular lifetime regime [29] and when $P_{\mathrm{AM}} \simeq 1$, ζ simplifies to $\Sigma_i f_i (4I_i + 2)^{-1}$, where f_i is the ith isotope's abundance and I_i is its nuclear spin. In the limits of $P_{\mathrm{AM}} \simeq 0$ and $P_{\mathrm{AM}} \simeq 1$, $\zeta_{\mathrm{Rb}} = 0.179$ and 0.095 and $\zeta_{\mathrm{Cs}} = 0.172$ and 0.0625, respectively. In the "very short" lifetime regime [29], $\zeta = 1/2$ (independent of P_{AM}). In Ref. [18], the short lifetime regime and $P_{\mathrm{AM}} \simeq 1$ were assumed. Our experiments are approaching (or within) the very short lifetime regime.

[35] Temperature dependencies of these terms are generally mild (e.g., $\langle \sigma v \rangle \propto T^{1/2}$) and are often neglected [18,29]—as with Γ_{Xe}, because $\Gamma_{\mathrm{Xe}} \ll \gamma_{\mathrm{SE}}$, $\Delta T/T \ll 1$, and its dependence may be nearly flat in our regime (e.g., Ref. [40]). Inclusion of the exponential dependence in Ref. [41] results in only small changes to our γ' values.

[36] S. Kadlecek, L. W. Anderson, and T. G. Walker, Phys. Rev. Lett. **80**, 5512 (1998).

[37] G. Tastevin, J. Low. Temp. Phys. **89**, 669 (1992); W. Heil *et al.*, Phys. Lett. A **201**, 337 (1995).

[38] N. Whiting, M. Barlow, H. Newton, L. Walkup, P. Nikolaou, and B. Goodson, in *2nd Experimental Nuclear Magnetic Resonance Conference* (Pacific Grove, CA, 2011).

[39] Z. I. Cleveland *et al.*, J. Chem. Phys. **124**, 044312 (2006);Stupic *et al.*, J. Magn. Reson. **208**, 58 (2011).

[40] I. A. Nelson, Ph.D. thesis, University of Wisconsin, 2001.

[41] B. Driehuys, G. D. Cates, and W. Happer, Phys. Rev. Lett. **74**, 4943 (1995).

[42] M. Rosen (personal communication).

[43] M. V. Romalis, E. Miron, and G. D. Cates, Phys. Rev. A **56**, 4569 (1997).